Pilot Protection Based on Backward Traveling-wave Voltage Difference for Submarine Cables of Low-frequency Transmission System with Integrated Offshore Wind Power

Xiaoping Gao, *Student Member*, *IEEE*, Guobing Song, *Senior Member*, *IEEE*, Xiaoning Kang, *Member*, *IEEE*, Can Cui, and Jifei Yan

Abstract—**Multiterminal low-frequency transmission system (LFTS) has promising potential for large-scale offshore wind power integration. Nevertheless, the existing protection suffers from low sensitivity, and even operates incorrectly because the converters connected to both ends of cables change fault characteristics substantially. To address this problem, this paper firstly inspects the adaptability of current differential protection, revealing the manner in which control strategies after fault impact the sensitivity of the existing protection. Then, based on the characteristics of armored three-core cable, phase-mode transformation is utilized to decouple the fault information and the specific moduli are selected to reflect all kinds of fault types. The expression of backward traveling-wave (BTW) voltage based on interpolation is derived under the condition of low sampling frequency. Finally, a pilot protection based on BTW voltage difference for submarine cables of LFTS with integrated offshore wind power is proposed, which has higher sensitivity because the difference between BTW calculated from local information and the one from remote information is considerable during fault transient period. Simulation tests compare the performance of the existing protection with that of the proposed protection. Extensive simulations corroborate that the proposed protection reliably identifies the fault cable in various fault scenarios.**

Index Terms—**Low-frequency transmission system, submarine cable, adaptability, wind power, traveling-wave voltage, pilot protection, differential protection.**

Nomenclature

A. Variables

Δt	Sampling interval
τ	Time that traveling wave takes to travel along cable
γ_φ	Propagation constant under modulus φ
A_φ	Propagation function under modulus φ
$B_{k,\varphi}$	Backward traveling-wave (BTW) voltage under modulus φ at relay k
$F_{k,\varphi}$	Forward traveling-wave (FTW) voltage under modulus φ at relay k
G_φ, C_φ	Shunt conductance and capacitance under modulus φ
I_m, I_n	Currents captured by relays m and n
I_{OWi}	Current provided by the i^{th} offshore wind power plant (OWPP)
I_{M3C}	Current provided by modular multilevel matrix converter (M3C)
I_{f1}	Current of short-circuit branch
I_{op}	Start-up current of current differential protection
I_d, I_r	Differential and restrained currents
I_a	Current flowing through conductor a
$I_{k,\varphi}$	Current under modulus φ at relay k
I_N	Rated current of OWPP
i_φ	Instantaneous current of phase φ
k_{res}	Restraint coefficient
k_i, p_i	The i^{th} residue and pole of $Z_{C,\varphi}$
l	Distance between relays m and n
l_i, q_i	The i^{th} residue and pole of $A_\varphi e^{s\tau}$
N	Sampling number during a time window
n	Current sampling order
N_S	Number of samples in a low frequency cycle
r_{err}	Error of Marti model
r_{Thre}	Threshold of protection criterion
R_{f1}	Fault resistance
R_φ, L_φ	Series resistance and inductance under modulus φ

Manuscript received: April 28, 2024; revised: August 2, 2024; accepted: November 7, 2024. Date of CrossCheck: November 7, 2024. Date of online publication: December 4, 2024.

This work was supported by the National Key Research and Development Program of China (No. 2021YFB2401100).

X. Gao, G. Song (corresponding author), X. Kang, C. Cui, and J. Yan are with the School of Electric Engineering, Xi'an Jiaotong University, Xi'an, China (e-mail: xpgao123@stu.xjtu.edu.cn; song.gb@mail.xjtu.edu.cn; kangxn@xjtu.edu.cn; 2204112335@stu.xjtu.edu.cn; yanjf@stu.xjtu.edu.cn).

DOI: 10.35833/MPCE.2024.000448

R_i, C_i	Resistance and capacitance of the i^{th} resistance-capacitance parallel block
s_{cd}	Sensitivity of current differential protection
s_{Marti}	Sensitivity of pilot protection based on Marti model
$\boldsymbol{T}_i$, $\boldsymbol{T}_u$	Current and voltage decoupling matrices
t_{ij}	Element of $\boldsymbol{T}_i$
U_{m}, U_{n}	Voltages captured by relays m and n
U_{fl}	Voltage of fault point
U_{M3C}	Voltage provided by M3C
U_{a}	Voltage of conductor a
$U_{k,\varphi}$	Voltage under modulus φ at relay k
U_i	Voltage drop along the i^{th} resistance-capacitance parallel block
$y_{\text{a,b}}$	Admittance between conductors a and b
w	Angular frequency
$Z_{\text{cable1,m}}$	Impedance from fault point to relay m
$Z_{\text{cable1,n}}$	Impedance from fault point to relay n
$Z_{\text{cable}i}$	Impedance of the i^{th} cable
$Z_{\text{T,OW}i}$	Impedance of main transformer in the i^{th} OWPP
$Z_{\text{T,M3C}}$	Impedance of isolation transformer in M3C
$z_{\text{a,b}}$	Impedance between conductors a and b
$Z_{C,\varphi}$	Characteristic impedance under modulus φ

B. Superscripts

+, –, 0	Positive-, negative-, and zero-sequence components

C. Subscripts

A, B, C, M	Conductors A, B, C, and armor of armored three-core cables (ATCs)
SA, SB, SC	Metallic sheaths A, B, and C of ATCs

I. Introduction

OFFSHORE wind power has attracted much attention for its advantages of steady wind velocity and lower environmental implication [1], which is regarded as a potential alternative to fossil energy and has been built on a considerable scale in Europe and China. Low-frequency transmission system (LFTS) [2], [3] combines the benefits of direct current (DC) [4], [5] and alternating current (AC) transmission systems [6], which enhances transmission capability via drastically decreasing the transmission frequency and diminishing capacitive current of cables. At the same time, the investment in the offshore converter station is saved. The scale of multiterminal LFTS could be expanded conveniently compared with multiterminal AC transmission system, and the technical bottleneck such as expensive DC breakers in DC system is no longer a concern for LFTS [7]. To integrate wind energy located over 70 km offshore, multiterminal LFTS has a promising application prospect. Modular multilevel matrix converter (M3C) is a core equipment of LFTS, which connects with a power-frequency grid and aims to provide voltage support for offshore wind power plants (OWPPs). It is regarded as the extension of modular multilevel converter (MMC) and inherits advantages such as flexible power factor adjustment, low harmonic levels, and power supply capacity for passive grids [8], [9]. Submarine cables work in a harsh environment and are susceptible to external forces such as maritime activities and chemical pollution, which leads to the damage of the metallic sheath and armor layer, as well as insulation breakdown. Submarine cable fault is a menace to the safe operation of LFTS.

During the period of electromagnetic transients, fault analysis usually utilizes Thevenin's theorem to represent the synchronous generators as a constant voltage source with inductive impedance [10]. As for converter-based grid, electromagnetic transient and electromechanical transient overlap, so values of the power supply and impedance of converters change and the traditional analysis method is no longer valid. In this respect, adaptability may be a challenge for conventional protections in LFTS. Present studies of AC transmission line protection in converter-based system can be categorized to two types: non-unit protections and pilot protections.

The adaptability of traditional distance protection is evaluated and flexible controls of power electronic equipment are proved to be the dominant factor causing the distance protection operating incorrectly in [11]-[13]. A high-frequency voltage is modulated by MMC to structure equations containing fault distance for asymmetrical faults [14]. The control for symmetrical faults needs to be designed separately. Reference [15] modifies the fault current of converters to imitate the behavior of synchronous generators to ensure existing distance relays operate properly without any change. An overcurrent protection based on the negative-sequence currents (NSCs) provided by MMC is proposed in [16]. However, these control-based solutions demand redesign of the control system of converters, which will not be practical since most existing inverters are proprietary design. An adaptive distance protection based on the sequence network analysis considering different grid codes is proposed in [17], which calculates the equivalent impedance of remote system with local electrical quantities. However, this method will be invalid in LFTS because both ends of cables are connected with converters. Reference [18] proposes a time-domain distance protection independent of source characteristics. However, when the fault is not a bolted fault, the method needs communication.

High-voltage cables are mostly pipe-type cables, and the electromagnetic coupling in multi-conductors make the aforementioned distance protections inapplicable in LFTS. Overcurrent protection may bring about selectivity problem between upstream and downstream relays.

Reference [19] indicates fault currents provided by wind power plants and MMCs are quite different because different control strategies are adopted. It proposes a singularity-based protection, which performs well for short transmission lines. However, as for long cables, grounding capacitive currents change sharply under external faults. Hence, the singular values of currents at both ends of the line are not the same any more, which brings difficulties to the protection settings. Reference [20] reveals the magnitude differences of transient NSC between the faulty and healthy cables, but the information of all lines is required to identify the fault. Reference [21] introduces a novel protection based on similarity of currents, which performs well for converter-based girds. The capacitance value of submarine cables is tens of times larger than that of overhead lines, therefore the cosine similarity is no longer −1 when an external fault occurs. The method will bring about the difficulty for relay settings when applied in LFTS. References [22]-[24] propose differential protections based on traveling waves while ignoring the frequency-dependent characteristics of lines. Frequency-dependent characteristics of submarine cables are more obvious than overhead lines, which is worth noting during fault transient period.

A Marti model-based current differential protection is proposed for overhead lines in [25]. The local relay needs to obtain both three-phase voltages and currents at the remote end and compare the calculated values with measured values, which requires a high-bandwidth communication. Reference [26] modifies the NSC order of MMC to guarantee that current differential protection operates correctly. However, on the one hand, it may not be practical because the design of control system is proprietary of manufacturers and beyond the reach of utilities. On the other hand, the accompanying risk of overvoltage should be considered [16]. Reference [27] proposes a unit protection with model-recognition in frequency domain; however, the internal fault model is no longer inductive because the impedance of the converter is strongly coupled with the control. Phasor-based protections rely on the stable frequency that system supplies. Both ends of the cable in LFTS are connected with power electronic devices, including grid-side converter (GSC) of wind power plants and M3C. In other words, the penetration rate of power electronic devices reaches 100% at the low-frequency side. Therefore, it needs a considerable time for the converters to supply the stable frequency after faults because of the longer dynamic response of the control system, which reduces the operating speed of phasor-based protection and even leads to incorrect operations.

In addition to the above, existing protections of converter-based power system mainly focus on three-phase system; however, the coupling in multi-conductors of pipe-type cables cannot be ignored especially during the faut transient period.

The main objective of this study is to explore the factors influencing the reliability or sensitivity of the existing protection, then focus on the transient features of the protected armored three-core cables (ATCs) and propose an easy-to-implement protection independent of converter control strategies. The contributions of this paper are summarized as follows.

1) For the widely adopted current differential protection, the expressions of differential and restrained currents are derived using fault composite sequence networks. It is indicated that the sensitivity of the existing protection is strongly correlated to NSCs provided by GSC and M3C. The lower the NSCs are injected, the lower the sensitivity is, which will cause mal-operation of relays.

2) A time-domain decoupling method of fault information for ATC is introduced. And the specific modulus that can reflect all kinds of fault types is selected to extract fault transient characteristics.

3) A pilot protection based on backward traveling-wave (BTW) voltage difference is proposed, which is not influenced by converter control strategies. In order to implement the proposed protection even with low sampling frequency, the expression of BTW voltage is derived based on accurate interpolation.

The remainder of this paper is organized as follows. Section II presents adaptability analysis of existing current differential protections. Section III introduces a time-domain decoupling method of fault information for ATC and analyzes the fault characteristics of LFTS during transient period. In Section IV, the expression of BTW voltage based on accurate interpolation is derived. On this basis, a pilot protection based on BTW voltage difference for submarine cables in LFTS is proposed. Section V provides a comparison between existing protections and the proposed one. Finally, the conclusions are presented in Section VI.

II. Adaptability Analysis of Existing Current Differential Protection

This section gives a concise overview of LFTS and analyzes the adaptability of the current differential protection.

A. System Under Study

Figure 1 presents the topology of multiterminal LFTS with integrated OWPPs. Low-frequency power generated from wind plants is transmitted to the M3C via submarine cables. Then, the M3C increases the low frequency (50/3 or 20 Hz) to the power frequency (50 or 60 Hz). The low-frequency side of M3C is set as the grid-forming mode to provide voltage and frequency support, while GSCs and high-frequency side of M3C are set as the grid-following mode to transmit the maximum power of OWPPs.

To facilitate the cable laying, ATCs are widely used, of which the cross-section is displayed in Fig. 1.

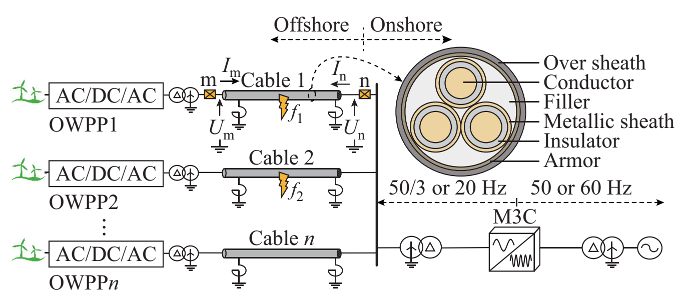

Fig. 1. Topology of multiterminal LFTS with integrated OWPPs.

The main transformers of OWPPs and the isolation transformers of M3C widely adopt dYG connection to block the path of zero-sequence currents. Generally, the high-voltage side adopts YG winding.

B. Adaptability Analysis

Current differential protection is widely adopted as main protection for AC lines (≥110 kV), which isolates internal faults reliably and rapidly [28]. This subsection focuses on the impact of converter control strategies on the fault current characteristics and further on current differential protections.

The capacitive current is greatly reduced thanks to the low frequency (only one third of the power frequency), while shunt reactors provide effective compensation. Therefore, shunt reactors and cable capacitance can be neglected in the following analysis. When a single-phase-to-ground fault occurs on cable 1, the composite sequence network is shown in Fig. 2.

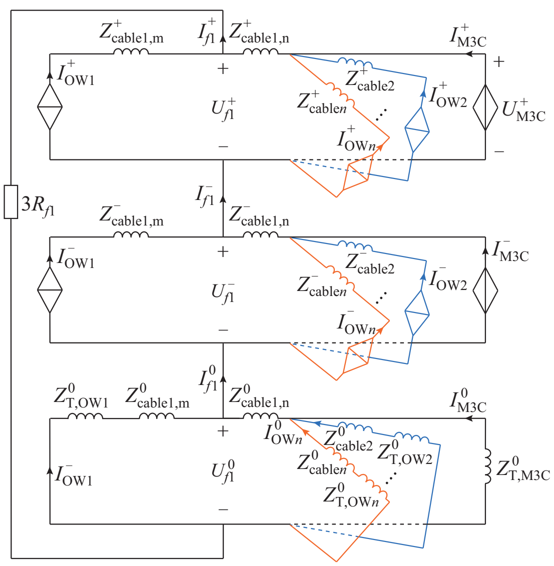

Fig. 2. Composite sequence network under a single-phase-to-ground fault.

The low-frequency side of M3C provides the voltage and frequency support for OWPPs and is thus considered as a voltage source. GSCs operate in the grid-following mode and are hence considered as current sources.

In Fig. 2, according to Kirchhoff's circuit laws and relationship between phase and sequence quantities, we have:

$$\begin{cases} I^+_{\text{M3C}}+\sum\limits_{i=1}^{n} I^+_{\text{OW}i}=I^-_{\text{M3C}}+\sum\limits_{i=1}^{n} I^-_{\text{OW}i}=I^0_{\text{M3C}}+\sum\limits_{i=1}^{n} I^0_{\text{OW}i} \\ I^0_{\text{OW1}}=I^0_{f1}\dfrac{Z^0_{\text{cable1,n}}+Z^0_{\text{T,M3C}}//Z_2//\ldots//Z_n}{Z_{\text{m}}+Z^0_{\text{cable1,n}}+Z^0_{\text{T,M3C}}//Z_2//\ldots//Z_n} \\ I_{\text{m}}=I^+_{\text{OW1}}+I^-_{\text{OW1}}+I^0_{\text{OW1}} \\ I_{\text{n}}=I^+_{\text{M3C}}+I^-_{\text{M3C}}+I^0_{\text{M3C}}+\sum\limits_{i=2}^{n}(I^+_{\text{OW}i}+I^-_{\text{OW}i}+I^0_{\text{OW}i}) \end{cases} \tag{1}$$

where $Z_{\text{m}}=Z^0_{\text{T,OW1}}+Z^0_{\text{cable1,m}}$; and $Z_i=Z^0_{\text{cable}i}+Z^0_{\text{T,OW}i}$ $(i=2,3,\ldots,n)$.

The operation criterion of practical current differential protections for the fault phase is expressed as:

$$\begin{cases} \left|I_{\text{m}}+I_{\text{n}}\right|>I_{\text{op}} \\ \left|I_{\text{m}}+I_{\text{n}}\right|>k_{\text{res}}\left|I_{\text{m}}-I_{\text{n}}\right| \end{cases} \tag{2}$$

Substituting (1) into (2), we have:

$$\begin{cases} I_{\text{d}}=\left|I_{\text{m}}+I_{\text{n}}\right|=\left|3\left(\sum\limits_{i=1}^{n} I^-_{\text{OW}i}+I^-_{\text{M3C}}\right)\right| \\ I_{\text{r}}=\left|I_{\text{m}}-I_{\text{n}}\right|=\left|\left(I^-_{\text{M3C}}+\sum\limits_{i=1}^{n} I^-_{\text{OW}i}\right)(k-2)+2I^-_{\text{OW1}}+2I^+_{\text{OW1}}\right| \\ k=\dfrac{Z^0_{\text{cable1,n}}+Z^0_{\text{T,M3C}}//Z_2//\ldots//Z_n-Z_{\text{m}}}{Z^0_{\text{cable1,n}}+Z^0_{\text{T,M3C}}//Z_2//\ldots//Z_n+Z_{\text{m}}} \end{cases} \tag{3}$$

According to (1)-(3), the differential current depends only on NSCs of GSCs and M3C, while the restrained current is affected by positive-sequence current I^+_{OW1} as well. Therefore, the sensitivity of current differential protection is strongly correlated to NSCs provided by converters. The lower the NSCs injected, the lower the sensitivity. In fact, both GSCs and M3C suppress their NSCs to ensure the power quality [29], [30]. The differential current is theoretically controlled at zero, which will cause a mal-operation of current differential protections for internal faults. Similarly, the challenge still exists for a phase-to-phase fault because positive- and negative-sequence networks are connected in parallel according to their composite sequence networks.

In summary, unlike the synchronous generator system, when an internal fault occurs, the fault currents captured by the relays in the LFTS are no longer in phase and even exhibit fault characteristics similar to those in the isolated neutral system if NSCs are suppressed. It brings a huge challenge for traditional protections based on phasors. Besides, the reduction of transmission frequency in LFTS results in more time to extract phasors, which further reduces the operating speed of the protection. Thus, transient-based protection independent of control strategies is promising for LFTS.

III. Time-domain Decoupling Method of Fault Information for ATC and Fault Characteristic Analysis of LFTS During Transient Period

Phasor-based protection confronts the challenge of mal-operation. This section firstly introduces a time-domain decoupling method of fault information for ATC, and then analyzes the fault characteristics of LFTS during the transient period.

A. Time-domain Decoupling Method of Fault Information for ATC

In the sectional view of the ATC shown in Fig. 1, there are seven metallic layers, including three conductors, three metallic sheaths, and one armor. The phase electrical quantity cannot be analyzed separately due to the electromagnetic coupling in multi-conductors, which causes inconvenience for transient analysis. The impedance matrix $\boldsymbol{Z}$ and admittance matrix $\boldsymbol{Y}$ of ATC are represented as [31]:

$$\boldsymbol{Z}=\begin{bmatrix} z_{\text{A,A}} & z_{\text{A,SA}} & z_{\text{A,B}} & z_{\text{A,SB}} & z_{\text{A,C}} & z_{\text{A,SC}} & z_{\text{A,M}} \\ z_{\text{SA,A}} & z_{\text{SA,SA}} & z_{\text{SA,B}} & z_{\text{SA,SB}} & z_{\text{SA,C}} & z_{\text{SA,SC}} & z_{\text{SA,M}} \\ z_{\text{B,A}} & z_{\text{B,SA}} & z_{\text{B,B}} & z_{\text{B,SB}} & z_{\text{B,C}} & z_{\text{B,SC}} & z_{\text{B,M}} \\ z_{\text{SB,A}} & z_{\text{SB,SA}} & z_{\text{SB,B}} & z_{\text{SB,SB}} & z_{\text{SB,C}} & z_{\text{SB,SC}} & z_{\text{SB,M}} \\ z_{\text{C,A}} & z_{\text{C,SA}} & z_{\text{C,B}} & z_{\text{C,SB}} & z_{\text{C,C}} & z_{\text{C,SC}} & z_{\text{C,M}} \\ z_{\text{SC,A}} & z_{\text{SC,SA}} & z_{\text{SC,B}} & z_{\text{SC,SB}} & z_{\text{SC,C}} & z_{\text{SC,SC}} & z_{\text{SC,M}} \\ z_{\text{M,A}} & z_{\text{M,SA}} & z_{\text{M,B}} & z_{\text{M,SB}} & z_{\text{M,C}} & z_{\text{M,SC}} & z_{\text{M,M}} \end{bmatrix} \tag{4a}$$

$$\boldsymbol{Y}=\begin{bmatrix} y_{\mathrm{A,A}} & y_{\mathrm{A,SA}} & 0 & 0 & 0 & 0 & 0 \\ y_{\mathrm{SA,A}} & y_{\mathrm{SA,SA}} & 0 & y_{\mathrm{SA,SB}} & 0 & y_{\mathrm{SA,SC}} & y_{\mathrm{SA,M}} \\ 0 & 0 & y_{\mathrm{B,B}} & y_{\mathrm{B,SB}} & 0 & 0 & 0 \\ 0 & y_{\mathrm{SB,SA}} & y_{\mathrm{SB,B}} & y_{\mathrm{SB,SB}} & 0 & y_{\mathrm{SB,SC}} & y_{\mathrm{SB,M}} \\ 0 & 0 & 0 & 0 & y_{\mathrm{C,C}} & y_{\mathrm{C,SC}} & 0 \\ 0 & y_{\mathrm{SC,SA}} & 0 & y_{\mathrm{SC,SB}} & y_{\mathrm{SC,C}} & y_{\mathrm{SC,SC}} & y_{\mathrm{SC,M}} \\ 0 & y_{\mathrm{M,SA}} & 0 & y_{\mathrm{M,SB}} & 0 & y_{\mathrm{M,SC}} & y_{\mathrm{M,M}} \end{bmatrix} \tag{4b}$$

At the same time, the elements Z_{ij} and Y_{ij} $(1 \le i, j \le 7)$ satisfy:

$$\begin{cases} Z_{11}=Z_{33}=Z_{55} \\ Z_{12}=Z_{21}=Z_{22}=Z_{34}=Z_{43}=Z_{44}=Z_{56}=Z_{65}=Z_{66} \\ Z_{13}=Z_{14}=Z_{15}=Z_{16}=Z_{23}=Z_{24}=Z_{25}=Z_{26}=Z_{31}= \\ \quad Z_{32}=Z_{35}=Z_{36}=Z_{41}=Z_{42}=Z_{45}=Z_{46}=Z_{51}= \\ \quad Z_{52}=Z_{53}=Z_{54}=Z_{61}=Z_{62}=Z_{63}=Z_{64} \\ Z_{17}=Z_{27}=Z_{37}=Z_{47}=Z_{57}=Z_{67}=Z_{71}=Z_{72}=Z_{73}= \\ \quad Z_{74}=Z_{75}=Z_{76}=Z_{77} \\ Y_{11}=Y_{33}=Y_{55}=-Y_{12}=-Y_{21}=-Y_{34}=-Y_{43}=-Y_{56}=-Y_{65} \\ Y_{22}=Y_{44}=Y_{66} \\ Y_{24}=Y_{26}=Y_{42}=Y_{46}=Y_{62}=Y_{64} \\ Y_{27}=Y_{47}=Y_{67}=Y_{72}=Y_{74}=Y_{76} \end{cases} \tag{5}$$

According to the transmission line model, phase voltages and currents of ATC satisfy:

$$\begin{cases} \dfrac{\partial \boldsymbol{U}}{\partial x}=-\boldsymbol{ZI} \\ \dfrac{\partial \boldsymbol{I}}{\partial x}=-\boldsymbol{YU} \\ \boldsymbol{U}=[U_{\mathrm{A}}, U_{\mathrm{SA}}, U_{\mathrm{B}}, U_{\mathrm{SB}}, U_{\mathrm{C}}, U_{\mathrm{SC}}, U_{\mathrm{M}}]^{\mathrm{T}} \\ \boldsymbol{I}=[I_{\mathrm{A}}, I_{\mathrm{SA}}, I_{\mathrm{B}}, I_{\mathrm{SB}}, I_{\mathrm{C}}, I_{\mathrm{SC}}, I_{\mathrm{M}}]^{\mathrm{T}} \end{cases} \tag{6}$$

Furthermore, (6) can be transformed into a second-order partial differential equation:

$$\begin{cases} \dfrac{\partial^2 \boldsymbol{U}}{\partial x^2}=\boldsymbol{ZYU} \\ \dfrac{\partial^2 \boldsymbol{I}}{\partial x^2}=\boldsymbol{YZI} \end{cases} \tag{7}$$

Off-diagonal elements of $\boldsymbol{ZY}$ and $\boldsymbol{YZ}$ are not equal to 0, which causes the electromagnetic coupling. Diagonalize them to obtain the decoupled moduli, as shown in (8).

$$\begin{cases} \dfrac{\partial^2 \boldsymbol{U}_{\mathrm{m}}}{\partial x^2}=\boldsymbol{T}_u^{-1}\boldsymbol{ZYT}_u\boldsymbol{U}_{\mathrm{m}} \\ \dfrac{\partial^2 \boldsymbol{I}_{\mathrm{m}}}{\partial x^2}=\boldsymbol{T}_i^{-1}\boldsymbol{YZT}_i\boldsymbol{I}_{\mathrm{m}} \\ \boldsymbol{U}_{\mathrm{m}}=\boldsymbol{T}_u^{-1}\boldsymbol{U}=[U_\alpha, U_\beta, U_\gamma, U_\delta, U_\varepsilon, U_\zeta, U_\eta] \\ \boldsymbol{I}_{\mathrm{m}}=\boldsymbol{T}_i^{-1}\boldsymbol{I}=[I_\alpha, I_\beta, I_\gamma, I_\delta, I_\varepsilon, I_\zeta, I_\eta] \end{cases} \tag{8}$$

where subscripts α, β, γ, δ, ε, ζ, and η denote the elements of moduli.

Since the elements of $\boldsymbol{Z}$ and $\boldsymbol{Y}$ are complex numbers, the diagonalizing transformation matrix of $\boldsymbol{YZ}$ is also a complex matrix, which complicates the calculation. It is necessary to normalize and transform $\boldsymbol{T}_i$ into real numbers for practical applications. First, solve the complex diagonalizing transformation matrix $\boldsymbol{T}_i$, and then convert it to the real decoupling matrix $\boldsymbol{T}_{i,r}$. The relationship between them is shown in (9). The function real(·) is used to extract the real part of a complex number.

$$\boldsymbol{T}_{i,r}=\left(\mathrm{real}\left(\frac{t_{ij}}{\max\limits_{k\in\{1,2,\dots,7\}} t_{kj}}\right)\right) \quad 1\le i,j\le 7 \tag{9}$$

Accordingly, the real decoupling matrix $\boldsymbol{T}_{u,r}$ can be calculated as:

$$\boldsymbol{T}_{u,r}=(\boldsymbol{T}_{i,r}^{-1})^{\mathrm{T}} \tag{10}$$

Since the metallic sheaths and the armor are grounded together through low resistors at both ends, only the sum of the currents flowing through the metallic sheaths and the armor is practically measurable. Therefore, although there are theoretically seven current moduli according to (8), only specific mode currents are available. Taking HYJQF41-F-127/220kV ATC for instance, according to its current decoupling matrix, only I_α, I_δ, I_ε, and I_η are available. Furthermore, when a symmetric fault occurs, I_α is theoretically equal to zero. Therefore, although I_α is available, the value is too small. Status of each current modulus under different fault types is shown in Table I. In order to identify all kinds of fault types, only modulus δ, ε, and η are competent.

TABLE I
STATUS OF EACH CURRENT MODULUS UNDER DIFFERENT FAULT TYPES

Fault type	Current modulus						
	α	β	γ	δ	ε	ζ	η
No fault	○	×	×	√	√	×	√
A-SA	√	×	×	√	√	×	√
A-SA-M	√	×	×	√	√	×	√
A-SA-M-G	√	×	×	√	√	×	√
A-SA-SB	√	×	×	√	√	×	√
A-SA-B-SB	√	×	×	√	√	×	√
A-SA-B-SB-M	√	×	×	√	√	×	√
A-SA-B-SB-M-G	√	×	×	√	√	×	√
A-SA-B-SB-SC	√	×	×	√	√	×	√
A-SA-B-SB-C-SC	○	×	×	√	√	×	√
A-SA-B-SB-C-SC-M	○	×	×	√	√	×	√
A-SA-B-SB-C-SC-M-G	○	×	×	√	√	×	√

In Table I, √ denotes the modulus is available; × denotes the modulus is not available; ○ denotes the modulus is available, which is theoretically equal to zero; and fault type A-SA-M-G denotes short circuit fault among conductor A, metallic sheath A, armor M, and ground G. The other fault types follow the same rule.

B. Fault Characteristic Analysis of LFTS During Transient Period

The general solution of the wave equations (8) shows that the modulus voltage at any point is the superposition of two attenuating waves: forward traveling-wave (FTW) and BTW.

They propagate towards opposite directions, as shown in Fig. 3.

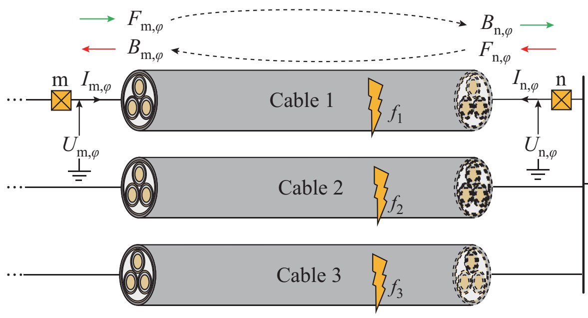

Fig. 3. Traveling-wave schematic diagram of ATCs.

The expressions of FTW and BTW voltages $F_{k,\varphi}$ and $B_{k,\varphi}$ are as follows:

$$\begin{cases} F_{k,\varphi}=\dfrac{1}{2}(U_{k,\varphi}+Z_{C,\varphi}I_{k,\varphi}) \\ B_{k,\varphi}=\dfrac{1}{2}(U_{k,\varphi}-Z_{C,\varphi}I_{k,\varphi}) \\ Z_{C,\varphi}=\sqrt{(R_\varphi+\mathrm{j}wL_\varphi)/(G_\varphi+\mathrm{j}wC_\varphi)} \end{cases} \tag{11}$$

For cable 1, when an external fault f_2 or f_3 occurs, FTW and BTW voltages satisfy (12) obviously.

$$\begin{cases} B_{\mathrm{m},\varphi}=F_{\mathrm{n},\varphi}A_\varphi \\ B_{\mathrm{n},\varphi}=F_{\mathrm{m},\varphi}A_\varphi \\ A_\varphi=\mathrm{e}^{-\gamma_\varphi l} \\ \gamma_\varphi=\sqrt{(R_\varphi+\mathrm{j}wL_\varphi)(G_\varphi+\mathrm{j}wC_\varphi)} \end{cases} \tag{12}$$

When an internal fault f_1 occurs, (12) is no longer valid since the fault breaks the balance of the equation. The difference between $B_{\mathrm{m},\varphi}$ and $F_{\mathrm{n},\varphi}A_\varphi$ is significant during fault transient period because the energy exchange between the capacitance and inductance in submarine cables dominates the characteristics and magnifies the fault current. The difference diminishes gradually when the control systems of converters come into play and weaken the fault characteristics. Taking full advantage of the fault characteristics during this period prevents the protection from the impact of control strategies.

IV. Proposed Pilot Protection

In order to exploit transient information under low sampling frequency conditions, this section firstly derives the expression of BTW voltage based on interpolation, and then introduces the proposed pilot protection for submarine cables of LFTS.

A. Calculation of BTW Voltage Based on Interpolation

Transient processes in the power system are most effectively analyzed in the time domain, therefore this subsection presents time-domain expressions for traveling waves.

1) FTW and BTW Voltages Based on Marti Model

R_φ and L_φ in (11) are frequency-dependent parameters due to the skin effect, so converting the frequency characteristics to time domain is the key. Marti model replaces $Z_{C,\varphi}$ with an equivalent network composed by resistance-capacitance parallel blocks, which have the same frequency response as $Z_{C,\varphi}$ [32]. In this paper, the vector fitting procedure is applied for rational function approximation to obtain the parameters of resistance and capacitance [33], as shown in (13).

$$\begin{cases} Z_{C,\varphi}(s)=k_0+\dfrac{k_1}{s+p_1}+\dfrac{k_2}{s+p_2}+\ldots+\dfrac{k_n}{s+p_n} \\ R_i=k_i/p_i \quad i=1,2,\ldots,n \\ C_i=1/k_i \quad i=1,2,\ldots,n \end{cases} \tag{13}$$

$Z_{C,\varphi}I_{k,\varphi}$ in (11) denotes the voltage drop across resistance-capacitance parallel blocks when $I_{k,\varphi}$ flows through it, hence its calculation in the time domain is:

$$\begin{cases} Z_{C,\varphi}I_{k,\varphi}(t)=U_{Z_C}(t)=k_0I_{k,\varphi}(t)+\sum\limits_{i=1}^{n}U_i(t) \\ U_i(t)=m_{1i}U_i(t-\Delta t)+m_{2i}(I_{k,\varphi}(t)+I_{k,\varphi}(t-\Delta t)) \\ m_{1i}=(1-0.5p_i\Delta t)/(1+0.5p_i\Delta t) \\ m_{2i}=0.5k_i\Delta t/(1+0.5p_i\Delta t) \end{cases} \tag{14}$$

Substituting (14) into (11), the expressions of FTW and BTW voltages in the time domain are:

$$\begin{cases} F_{k,\varphi}(t)=\dfrac{1}{2}\left(U_{k,\varphi}(t)+k_0I_{k,\varphi}(t)+\sum\limits_{i=1}^{n}U_i(t)\right) \\ B_{k,\varphi}(t)=\dfrac{1}{2}\left(U_{k,\varphi}(t)-k_0I_{k,\varphi}(t)-\sum\limits_{i=1}^{n}U_i(t)\right) \end{cases} \tag{15}$$

2) Improved Calculation of Convolution with Interpolation

In order to improve the calculation accuracy, the vector fitting procedure is also applied to fit the product of propagation function A_φ and $\mathrm{e}^{s\tau}$. Then, transform the partial fractions to exponential terms in the time domain and convolve them with FTW calculated in the previous part using recursive convolutions. The calculation of $F_{k,\varphi}(t)*A_\varphi(t)$ in the time domain is:

$$\begin{cases} F_{k,\varphi}(t)*A_\varphi(t)=F_{k\_\varphi}(t)*[A_\varphi\mathrm{e}^{s\tau}\mathrm{e}^{-s\tau}](t)=\sum\limits_{i=1}^{n}b_i(t) \\ A_\varphi\mathrm{e}^{s\tau}(s)=\dfrac{l_1}{s+q_1}+\dfrac{l_2}{s+q_2}+\ldots+\dfrac{l_n}{s+q_n} \\ b_i(t)=g_ib_i(t-\Delta t)+\dfrac{1}{2}c_i(U_k(t-\tau)+U_{Z_C}(t-\tau))+ \\ \qquad \dfrac{1}{2}d_i(U_k(t-\tau-\Delta t)+U_{Z_C}(t-\tau-\Delta t)) \\ g_i=\mathrm{e}^{-q_i\Delta t} \\ c_i=l_i(1-h_i)/q_i \\ d_i=-l_i(g_i-h_i)/q_i \\ h_i=(1-g_i)/(q_i\Delta t) \end{cases} \tag{16}$$

where function [·] is used to extract the integer component.

However, in most cases, unless specially designed, τ is not integer multiples of the sampling interval Δt, that is, $U_k(t-\tau)$ and $U_{Z_C}(t-\tau)$ in (16) cannot be obtained from the sampling values directly, especially in the cases with low sampling frequency. Hence, their values are approximated by the adjacent sampling data using linear interpolation. The expression of $F_{k,\varphi}(t) * A_{\varphi}(t)$ is shown as:

$$\begin{cases} F_{k,\varphi}(t) * A_{\varphi}(t) = F_{k,\varphi}(t) * [A_{\varphi} \mathrm{e}^{s\tau} \mathrm{e}^{-s\tau}](t) = \sum_{i=1}^{n} b_i(t) \\ b_i(t) = g_i b_i(t-\Delta t) + \dfrac{1}{2} c_i [k_1 U_k(t-k_3\Delta t) + k_2 U_k(t-k_4\Delta t) + \\ \qquad k_1 U_{Z_C}(t-k_3\Delta t) + k_2 U_{Z_C}(t-k_4\Delta t)] + \\ \qquad \dfrac{1}{2} d_i [k_1 U_k(t-(k_3+1)\Delta t) + k_2 U_k(t-(k_4+1)\Delta t) + \\ \qquad k_1 U_{Z_C}(t-(k_3+1)\Delta t) + k_2 U_{Z_C}(t-(k_4+1)\Delta t)] \\ k_2 = \tau/\Delta t - [\tau/\Delta t] \\ k_1 = 1 - k_2 \\ k_3 = [\tau/\Delta t] \\ k_4 = k_3 + 1 \end{cases} \tag{17}$$

B. Fault Line Identification Method

According to the fault characteristic analysis in Section III-B, when an external fault occurs, local FTW voltage and remote BTW voltage satisfy (12). While as for an internal fault, a significant difference between BTW voltage and $F_{k,\varphi}(t) * A_{\varphi}(t)$ emerges. Therefore, taking relay m for instance, the two criteria can be represented as:

$$\begin{cases} B_{\mathrm{m},\varphi}(t) \neq F_{\mathrm{n},\varphi}(t) * A_{\varphi}(t) \\ F_{\mathrm{m},\varphi}(t) * A_{\varphi}(t) \neq B_{\mathrm{n},\varphi}(t) \end{cases} \tag{18}$$

The expression of $F_{\mathrm{m},\varphi}(t) * A_{\varphi}(t)$ includes historical data according to (16), so it is obvious that constructing the criteria with local BTW voltage achieves better operating speed than with local FTW voltage. Modulus δ has the ability to distinguish all kinds of fault types, therefore the time-domain criterion of relay m to identify the fault line is represented as:

$$r_{err}(k) = \frac{\sum_{k=1}^{N} \left| B_{\mathrm{m},\delta}(k) - F_{\mathrm{n},\delta}(k) * A_{\delta}(k) \right|}{\sum_{k=1}^{N} \left(\left| B_{\mathrm{m},\delta}(k) \right| + \left| F_{\mathrm{n},\delta}(k) * A_{\delta}(k) \right| \right)} > r_{Thre} \tag{19}$$

To increase the sensitivity of identification criterion, current changes are adopted as:

$$\left| i_{\varphi}(n) - i_{\varphi}(n-N_S) \right| \cdot 0.1 I_N \quad \varphi = \mathrm{A, B, C} \tag{20}$$

In order to prevent incorrect pick-ups due to interference, fault line identification is activated when the current changes exceed the threshold continuously five times.

C. Working Steps of Proposed Protection

The flow chart of the proposed protection is depicted in Fig. 4. First, sample phase currents to check whether or not the protection identification criteria are met. If the criteria are met, the workflow proceeds to the fault line identification step. Calculate BTW voltage at local end and FTW voltage at remote end using (11), and then calculate the convolution of FTW voltage and the propagation function at the remote end using (17) based on the linear interpolation. Finally, if the criterion (19) is satisfied, it is considered as an internal fault and the circuit breakers are tripped. If not, reset the protection.

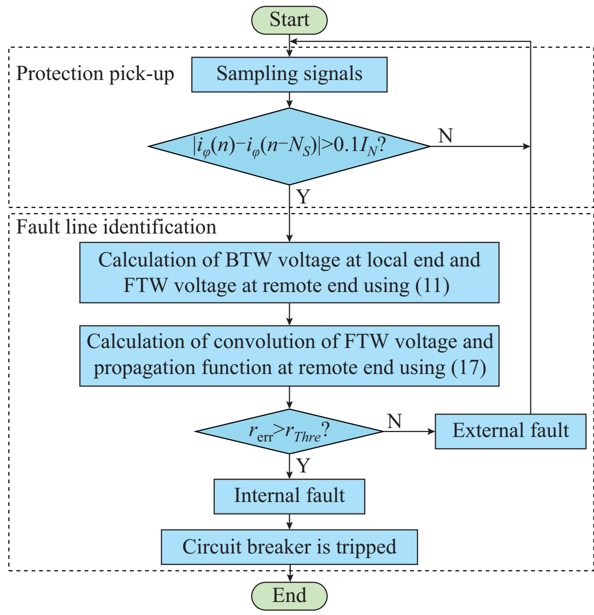

Fig. 4. Flowchart of proposed protection.

V. Simulation Verification

Extensive simulations are applied to check the performance between current differential protection and the proposed protection under various fault conditions. A multiterminal LFTS in Fig. 1 is established in PSCAD/EMTDC, which includes three OWPPs. In order to reduce simulation time, the OWPP is aggregated by the wind turbine generator with a multiplier element. And the numbers of wind turbine generators in the OWPPs 1, 2, and 3 are 25, 50, and 75, respectively. Table II presents the detailed parameters of LFTS under test. HYJQF41-F 127 kV/220 kV ATC is adopted, of which the armor and metallic sheaths are grounded at both ends. The numerical solution for its phase-mode transformation matrix is shown in (21), and modulus δ is used to identify the fault line.

$$\begin{cases} \boldsymbol{T}_{i,r}^{-1} = \\ \begin{bmatrix} 1 & 1 & 1 & 1 & 1 & 1 & 1 \\ -1 & -1 & -1 & -1 & -1 & -1 & 0 \\ 0.667 & 0.667 & -0.330 & -0.330 & -0.336 & -0.336 & 0 \\ 0.997 & 0 & 0.237 & 0 & 0.112 & 0 & 0 \\ 0.014 & 0 & -0.997 & 0 & -0.511 & 0 & 0 \\ 0 & 0 & 0.502 & 0.502 & -0.502 & -0.502 & 0 \\ 0 & 0 & 0 & 0 & 1 & 0 & 0 \end{bmatrix} \\ \boldsymbol{T}_{u,r}^{-1} = \\ \begin{bmatrix} 0 & 0 & 0 & 0 & 0 & 0 & 1 \\ 0 & -0.333 & 0 & -0.333 & 0 & -0.333 & 1 \\ 0 & 1 & 0 & -0.500 & 0 & -0.500 & 0 \\ 1 & -1 & 0.014 & -0.014 & 0 & 0 & 0 \\ 0.238 & -0.238 & -1 & 1 & 0 & 0 & 0 \\ 0 & -0.006 & 0 & 1 & 0 & -0.994 & 0 \\ 0.010 & -0.010 & -0.512 & 0.512 & 1 & -1 & 0 \end{bmatrix} \end{cases} \tag{21}$$

TABLE II
PARAMETERS OF LFTS UNDER TEST

Position	Item	Value
M3C	Rated capacity (MVA)	300
	Frequencies at both sides (Hz)	50/3, 50
	Rated voltages at both sides (kV)	220, 220
	Number of sub-modules per arm	200
	Rated voltage of sub-module (kV)	2
	Capacitance of sub-module (mF)	8
	Inductance of arm (mH)	100
	Converter transformer leakage reactance (p.u.)	0.1
GSC	Rated capacity (MVA)	2
	Voltage of DC side (kV)	1.7
	DC capacitance (mF)	15
	Step-up transformer leakage reactance (p.u.)	0.1
Cable	Lengths of cables 1, 2, and 3 (km)	100, 120, 140
	Capacities of shunt reactors of cables 1, 2, and 3 (Mvar)	29, 34, 40

A. Performance of Current Differential Protection

The performance of the current differential protection is checked when different orders of NSC are adopted by the M3C. This test aims to estimate the robustness of the current differential protection coping with different control strategies of converters. k_{res} is typically taken as 0.85 [26]. Figure 5 presents the simulation results of phase A for an internal A-SA-M-G fault with sampling frequency of 10 kHz and all faults are applied at 0 s. The operation criterion in (2) uses the one-cycle Fourier algorithm, while the distributed capacitance currents are compensated to obtain the currents at both ends.

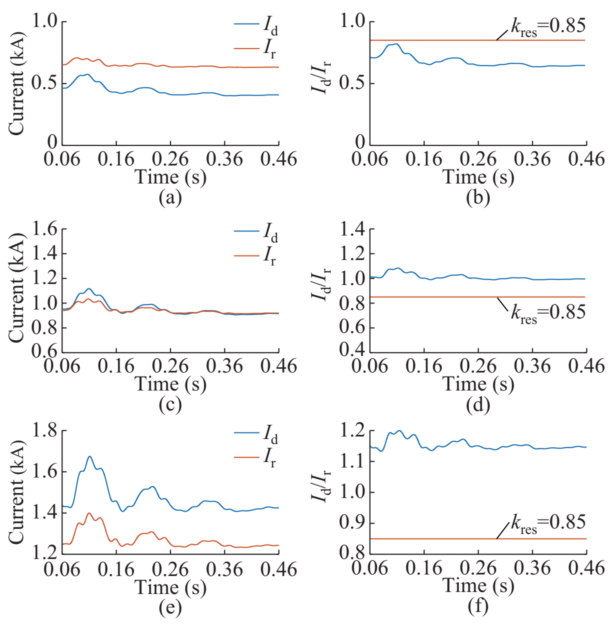

Fig. 5. Simulation results of phase A for internal A-SA-M-G fault. (a) I_d and I_r with NSC suppressed. (b) Ratio between I_d and I_r with NSC suppressed. (c) I_d and I_r when M3C injects NSC (0.05 p.u.). (d) Ratio between I_d and I_r when M3C injects NSC (0.05 p.u.). (e) I_d and I_r when M3C injects NSC (0.1 p.u.). (f) Ratio between I_d and I_r when M3C injects NSC (0.1 p.u.).

The NSC suppression of GSCs and M3C causes a mal-operation as shown in Fig. 5(b), since the restrained current I_r predominates rather than I_d. As NSC injected by M3C increases, the ratio between I_d and I_r increases, which contributes to correct operation of the current differential protection. Due to the dynamic characteristics of the Fourier algorithm, phasor-based protection needs to wait one cycle after the fault to perform calculations, which reduces the operating speed of the protection.

B. Performance of Proposed Protection

Comprehensive simulations are carried out to demonstrate the robustness of the proposed protection, including tests under different fault types, fault resistance, NSC orders of M3C, power levels, and fault occurrence time. Fault points f_1, f_2, and f_3 are set at midpoints of cables 1, 2, and 3, respectively. All tests are performed with a sampling frequency of 10 kHz. The time window is set to be 5 ms.

1) Performance Under Different Fault Types

In most cases of submarine cable faults, the fault resistance is low, typically less than 10 Ω [34], therefore the maximum value of the fault resistance is set to be 20 Ω. The threshold setting should ensure that the protection does not misoperate under external faults, while reliably identifying internal faults. In order to ensure adequate sensitivity for the detection of a slight fault with the maximum fault resistance, while allowing for a margin of error, the threshold value r_{Thre} in (19) is set to be 0.2. The simulation results under different fault types at relay m of cable 1 are shown in Fig. 6. The results show that the proposed protection can reliably identify the fault line under different fault types.

Taking the A-SA-SB-B-SC-C-M-G fault as an example, Fig. 7 displays the comparisons between $F_{n,\delta}(t)*A_\delta(t)$ and $B_{m,\delta}(t)$. The BTW voltage calculated from the local information is close to that calculated by the convolution of FTW voltage at remote end and $A_\delta(t)$ when an external fault occurs, which is not valid for an internal fault. The results confirm the conclusions of the fault characteristic analysis in Section III-B.

Identification results of different fault types are shown in Table III. r_{err} is the calculated value at 5 ms. It exceeds the threshold in 5 ms for internal faults with different fault resistance. While it is below the threshold for external faults, which indicates the reliability of the proposed protection.

The sensitivity is defined as the ratio of the operation quantity to the threshold. Table IV shows the sensitivity comparison between the current differential protection and the proposed protection for bolted internal faults. The current differential protection tends to malfunction due to the reduced sensitivity caused by NSC suppression, whereas the proposed protection has sufficient sensitivity to identify the fault line.

2) Performance Under Different NSC Orders

The proposed protection uses the information during the fault transient period. The difference between $B_{m,\varphi}(t)$ and $F_{n,\varphi}(t)*A_\varphi(t)$ is significant during this period even if both GSCs and the low-frequency side of M3C suppress their NSCs.

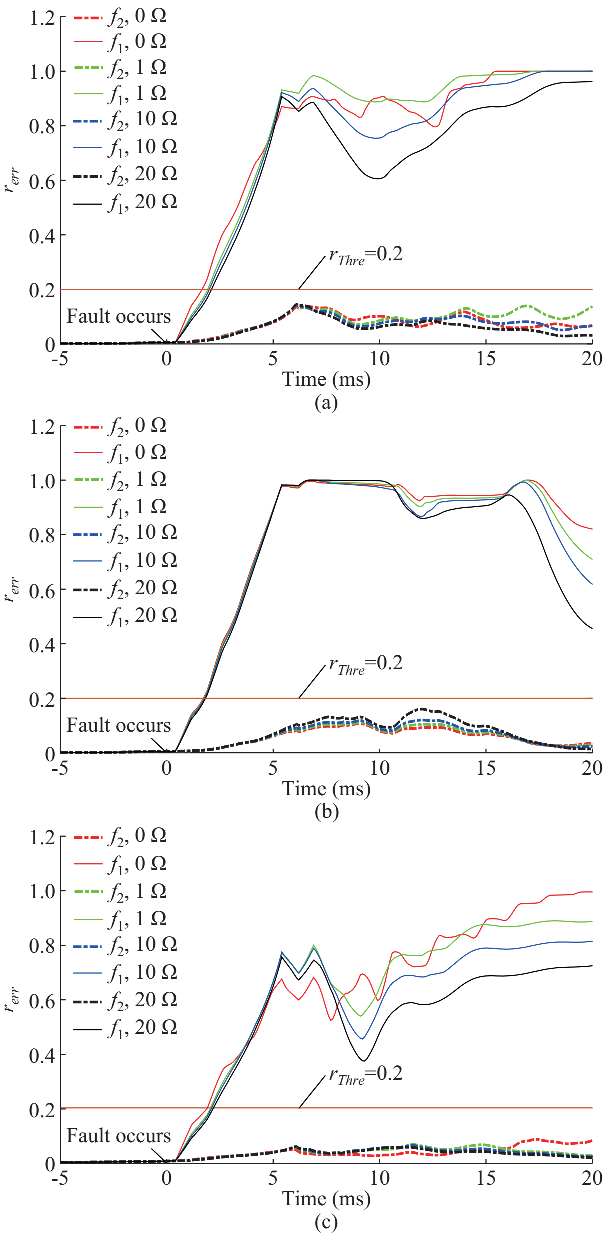

Fig. 6. Simulation results under different fault types at relay m of cable 1. (a) A-SA-M-G. (b) A-SA-B-SB. (c) A-SA-B-SB-C-SC-M-G.

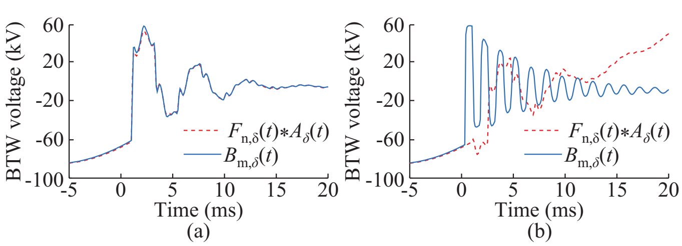

Fig. 7. Comparison between $F_{n,\delta}(t)*A_{\delta}(t)$ and $B_{m,\delta}(t)$ when A-SA-SB-B-SC-C-M-G fault occurs. (a) f_2 when fault resistance is 1 Ω. (b) f_1 when fault resistance is 1 Ω.

Figure 8 presents the simulation results under different NSCs injected by M3C (GSCs suppress their NSCs) when an A-SA-M-G fault occurs. The results show that the proposed protection correctly identifies the fault line regardless of NSC orders followed by M3C.

TABLE III
IDENTIFICATION RESULTS OF DIFFERENT FAULT TYPES

Fault type	Fault point	R_{f1} (Ω)	r_{err}	Identification result	Fault type	Fault point	R_{f1} (Ω)	r_{err}	Identification result
A-SA	f_1	0	0.7891	Internal	A-SA-B-SB-M-G	f_1	0	0.9098	Internal
		10	0.7350				10	0.8348	
		20	0.4973				20	0.7049	
	f_2	0	0.0789	External		f_2	0	0.0675	External
		10	0.0789				10	0.0584	
		20	0.0543				20	0.0559	
A-SA-M	f_1	0	0.7895	Internal	A-SA-B-SB-SC	f_1	0	0.9100	Internal
		10	0.7709				10	0.8347	
		20	0.5927				20	0.6755	
	f_2	0	0.0788	External		f_2	0	0.0676	External
		10	0.0821				10	0.0786	
		20	0.0651				20	0.0563	
A-SA-SB	f_1	0	0.7891	Internal	A-SA-B-SB-C-SC	f_1	0	0.6345	Internal
		10	0.7772				10	0.6493	
		20	0.6012				20	0.5867	
	f_2	0	0.0788	External		f_2	0	0.0392	External
		10	0.0821				10	0.0372	
		20	0.0661				20	0.0417	
A-SA-B-SB-M	f_1	0	0.9100	Internal	A-SA-B-SB-C-SC-M	f_1	0	0.6344	Internal
		10	0.8314				10	0.6493	
		20	0.6683				20	0.5867	
	f_2	0	0.0675	External		f_2	0	0.0392	External
		10	0.0788				10	0.0372	
		20	0.0559				20	0.0417	

TABLE IV
SENSITIVITY COMPARISON OF DIFFERENT PROTECTIONS

Fault type	s_{cd}	s_{Marti}
A-SA	0.8342	3.9455
A-SA-M	0.8345	3.9475
A-SA-M-G	0.8345	3.9465
A-SA-SB	0.8345	3.9455
A-SA-B-SB	1.9418	4.4730
A-SA-B-SB-M	1.9418	4.5500
A-SA-B-SB-M-G	1.9418	4.5490
A-SA-B-SB-SC	1.9418	4.5500
A-SA-B-SB-C-SC	1.2437	3.1725
A-SA-B-SB-C-SC-M	1.2437	3.1720
A-SA-B-SB-C-SC-M-G	1.2437	3.1720

3) *Performance Under Different Power Levels*

The rated capacities of the three OWPPs are different, so the power levels of the three cables are also different. Taking cables 2 and 3 as example, the simulation results under different power levels for A-SA-M-G fault are shown in Fig. 9, and the identification results under different fault resistances are shown in Table V. The results indicate that the proposed protection reliably identifies the fault line regardless of power levels.

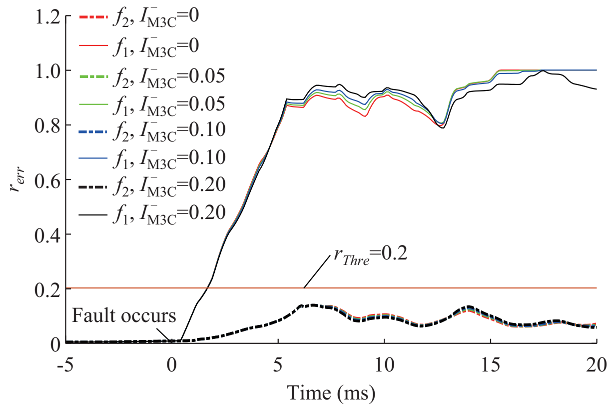

Fig. 8. Simulation results under different NSCs injected by M3C.

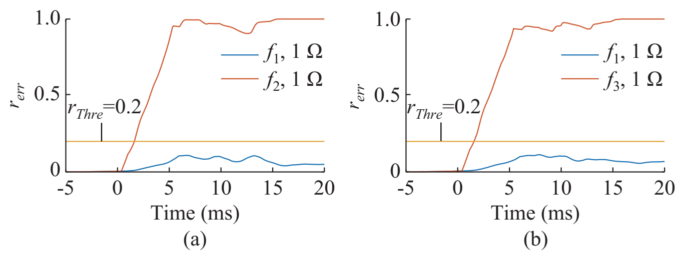

Fig. 9. Simulation results under different power levels for A-SA-M-G fault. (a) Cable 2. (b) Cable 3.

TABLE V
IDENTIFICATION RESULTS UNDER DIFFERENT FAULT RESISTANCES

Cable	Fault point	R_f (Ω)	r_{err}	Identification result
Cable 2	f_1	0	0.0637	External
		10	0.0805	
		20	0.0808	
	f_2	0	0.8480	Internal
		10	0.8100	
		20	0.6997	
Cable 3	f_1	0	0.0658	External
		10	0.0779	
		20	0.0903	
	f_3	0	0.8368	Internal
		10	0.8263	
		20	0.7461	

4) Performance Under Different Fault Occurrence Time

In order to test the performance of the proposed protection under different fault occurrence time, faults are set under different voltage angles. Take A-SA-M-G fault for instance, when faults occur under various voltage angles of phase A, simulation results at relay m of cable 1 are shown in Fig. 10. All fault time is offset to 0 s for ease of observation. Simulation results under other voltage angles are presented in Table VI. The results verify that the proposed protection is valid regardless of fault occurrence time.

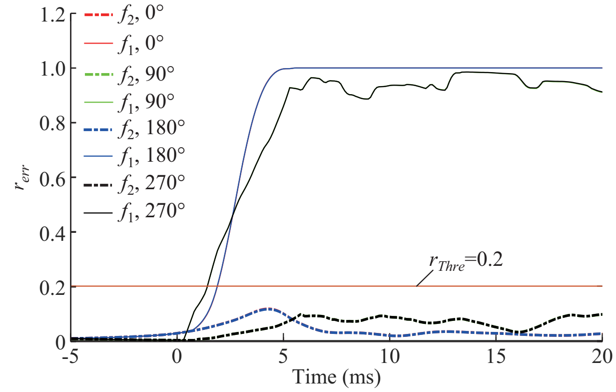

Fig. 10. Simulation results under different voltage angles for A-SA-M-G fault.

TABLE VI
RESULTS UNDER DIFFERENT VOLTAGE ANGLES

Voltage angle (°)	Fault point	R_f (Ω)	r_{err}	Identification result
45	f_1	0	0.9070	Internal
		1	0.9078	
	f_2	0	0.0608	External
		1	0.0657	
135	f_1	0	0.8136	Internal
		1	0.8283	
	f_2	0	0.0721	External
		1	0.0744	
225	f_1	0	0.9069	Internal
		1	0.9078	
	f_2	0	0.0609	External
		1	0.0657	
315	f_1	0	0.8138	Internal
		1	0.8282	
	f_3	0	0.0722	External
		1	0.0745	

VI. CONCLUSION

For submarine cables where both ends are connected to converters, the traditional phasor-based pilot protection is susceptible to insufficient sensitivity, and may even malfunction due to inappropriate control strategies.

On basis of the fault characteristics of ATC during fault transient period, a pilot protection based on BTW voltage difference for submarine cables of LFTS is proposed. The following conclusions can be drawn.

There is a strong correlation between the differential current and the NSC injected by converters under asymmetric faults. Small NSCs often cause mal-operations of relays. Furthermore, the process of phasor extraction reduces the operating speed of conventional protections, especially in LFTS. The expression of BTW voltage based on interpolation can be applied to the scenario of low sampling frequency, which reduces the sampling demand. The proposed protection for submarine cables operates correctly, independent of control strategies. Numerous simulation tests verify that it could identify the fault line reliably in 5 ms with a high sensitivity.

REFERENCES

[1] H. Lin, T. Xue, J. Lyu *et al*., "Impact of different AC voltage control modes of wind-farm-side MMC on stability of MMC-HVDC with offshore wind farms," *Journal of Modern Power Systems and Clean Energy*, vol. 11, no. 5, pp. 1687-1699, Sept. 2023.

[2] X. Wang and X. Wang, "Feasibility study of fractional frequency transmission system," *IEEE Transactions on Power Systems*, vol. 11, no. 2, pp. 962-967, May 1996.

[3] X. Wang, C. Cao, and Z. Zhou, "Experiment on fractional frequency transmission system," *IEEE Transactions on Power Systems*, vol. 21, no. 1, pp. 372-377, Feb. 2006.

[4] H. Zheng, X. Yuan, J. Cai *et al*., "Large-signal stability analysis of DC side of VSC-HVDC system based on estimation of domain of attraction," *IEEE Transactions on Power Systems*, vol. 37, no. 5, pp. 3630-3641, Sept. 2022.

[5] S. Yu, X. Wang, and C. Pang, "A pilot protection scheme of DC lines for MMC-HVDC grid using random matrix," *Journal of Modern Power Systems and Clean Energy*, vol. 11, no. 3, pp. 950-966, May 2023.

[6] G. Song, C. Wang, T. Wang *et al*., "A phase selection method for wind power integration system using phase voltage waveform correlation," *IEEE Transactions on Power Delivery*, vol. 32, no. 2, pp. 740-748, Apr. 2017.

[7] S. Liu, X. Wang, L. Ning *et al*., "Integrating offshore wind power via fractional frequency transmission system," *IEEE Transactions on Power Delivery*, vol. 32, no. 3, pp. 1253-1261, Jun. 2017.

[8] P. Bravo, J. Pereda, M. M. C. Merlin *et al*., "Modular multilevel matrix converter as solid state transformer for medium and high voltage AC substations," *IEEE Transactions on Power Delivery*, vol. 37, no. 6, pp. 5033-5043, Dec. 2022.

[9] Y. Meng, S. Li, Y. Zou *et al*., "Stability analysis and control optimisation based on particle swarm algorithm of modular multilevel matrix converter in fractional frequency transmission system," *IET Generation, Transmission & Distribution*, vol. 14, no. 14, pp. 2641-2655, Jul. 2020.

[10] S. Yu, Z. Zhou, X. Wang *et al*., "Adaptability analysis of power frequency variation distance protection for AC-side of receiving-end converter of offshore wind power MMC-HVDC system," in *Proceedings of 2022 4th International Conference on Smart Power & Internet Energy Systems*, Beijing, China, Dec. 2022, pp. 339-344.

[11] K. Jia, Z. Yang, Y. Fang *et al*., "Influence of inverter-interfaced renewable energy generators on directional relay and an improved scheme," *IEEE Transactions on Power Electronics*, vol. 34, no. 12, pp. 11843-11855, Dec. 2019.

[12] A. Hooshyar, M. A. Azzouz, and E. F. El-Saadany, "Distance protection of lines emanating from full-scale converter-interfaced renewable energy power plants – part I: problem statement," *IEEE Transactions on Power Delivery*, vol. 30, no. 4, pp. 1770-1780, Aug. 2015.

[13] Y. Fang, K. Jia, Z. Yang *et al*., "Impact of inverter-interfaced renewable energy generators on distance protection and an improved scheme," *IEEE Transactions on Industrial Electronics*, vol. 66, no. 9, pp. 7078-7088, Sept. 2019.

[14] T. Zheng, W. Lv, X. Zhuang *et al*., "Improved time-domain distance protection for asymmetrical faults based on adaptive control of MMC in offshore AC network," *International Journal of Electrical Power & Energy Systems*, vol. 152, p. 109229, Oct. 2023.

[15] A. Banaiemoqadam, A. Hooshyar, and M. A. Azzouz, "A control-based solution for distance protection of lines connected to converter-interfaced sources during asymmetrical faults," *IEEE Transactions on Power Delivery*, vol. 35, no. 3, pp. 1455-1466, Jun. 2020.

[16] L. Shi, G. P. Adam, R. Li *et al*., "Control of offshore MMC during asymmetric offshore AC faults for wind power transmission," *IEEE Journal of Emerging and Selected Topics in Power Electronics*, vol. 8, no. 2, pp. 1074-1083, Jun. 2020.

[17] C. Chao, X. Zheng, Y. Weng *et al*., "Adaptive distance protection based on the analytical model of additional impedance for inverter-interfaced renewable power plants during asymmetrical faults," *IEEE Transactions on Power Delivery*, vol. 37, no. 5, pp. 3823-3834, Oct. 2022.

[18] P. Adhikari, S. Brahma, and P. H. Gadde, "Source-agnostic time-domain distance relay," *IEEE Transactions on Power Delivery*, vol. 37, no. 5, pp. 3620-3629, Oct. 2022.

[19] L. Zheng, K. Jia, B. Yang *et al*., "Singular value decomposition based pilot protection for transmission lines with converters on both ends," *IEEE Transactions on Power Delivery*, vol. 37, no. 4, pp. 2728-2737, Aug. 2022.

[20] T. Zheng, J. Ma, W. Lyu *et al*., "Protection for AC collection line of offshore wind power based on ratio of transient negative-sequence current accumulation," *Automation of Electric Power Systems*, vol. 47, no. 12, pp. 137-144, Jun. 2023.

[21] L. Zheng, K. Jia, T. Bi *et al*., "Cosine similarity based line protection for large-scale wind farms," *IEEE Transactions on Industrial Electronics*, vol. 68, no. 7, pp. 5990-5999, Jul. 2021.

[22] B. Chen, Y. Dai, X. Dong *et al*., "Traveling wave differential protection applied to renewable energy and flexible DC connected lines," in *Proceedings of 2023 IEEE International Conference on Advanced Power System Automation and Protection*, Xuchang, China, Oct. 2023, pp. 15-19.

[23] Z. Chen, X. Ding, Q. Gan *et al*., "Differential protection for double-ended weak-infeed transmission lines based on time-domain integral value of traveling waves," in *Proceedings of 2023 IEEE International Conference on Advanced Power System Automation and Protection*, Xuchang, China, Oct. 2023, pp. 447-451.

[24] X. Li, W. Li, B. Chen *et al*., "Traveling wave protection for the ac transmission lines between mmc stations and renewable energy sources," in *Proceedings of 2023 IEEE International Conference on Advanced Power System Automation and Protection*, Xuchang, China, Oct. 2023, pp. 140-144.

[25] Y. Qiao and C. Qing, "A novel current differential relay principle based on Marti model," in *Proceedings of 10th IET International Conference on Developments in Power System Protection*, Manchester, UK, Mar. 2010, pp. 1-6.

[26] T. Zheng, X. Zhuang, W. Lyu *et al*., "Negative sequence current reference selection and protection adaptability analysis of flexible DC converter station for offshore wind power," *Automation of Electric Power Systems*, vol. 47, no. 3, pp. 133-141, Feb. 2023.

[27] C. Wang, G. Song, X. Kang *et al*., "Novel transmission-line pilot protection based on frequency-domain model recognition," *IEEE Transactions on Power Delivery*, vol. 30, no. 3, pp. 1243-1250, Jun. 2015.

[28] T. Huang, H. Xie, X. Xu *et al.*, "Impact of converter control on differential protection under symmetrical fault and optimization strategy," *Proceedings of the CSEE*, vol. 44, no. 13, pp. 5063-5073, Jul. 2024.

[29] X. Wu, H. Zhu, Y. Dong *et al*., "Frequency-division and hierarchical control of modular multilevel matrix converter for flexible low-frequency transmission," *Automation of Electric Power Systems*, vol. 45, no. 18, pp. 131-140, Sept. 2021.

[30] X. Wang, W. Yang, Z. Shi *et al*., "Resonant based overvoltage restraining strategy for MMC-HVDC wind power transmission system under sending end grid fault," in *Proceedings of 2021 6th Asia Conference on Power and Electrical Engineering*, Chongqing, China, Apr. 2021, pp. 63-68.

[31] N. Peng, P Zhang, and R. Liang, "Fault sensing and location of the three-core armored cables in distribution network based on the analysis of the fault-featured transient moduli," *Proceedings of the CSEE*, vol. 41, no. 16, pp. 5767-5779, Aug. 2021.

[32] J. Marti, "Accurate modelling of frequency-dependent transmission lines in electromagnetic transient simulations," *IEEE Transactions on Power Apparatus Systems*, vol. 101, no. 1, pp. 147-157, Jan. 1982.

[33] B. Gustavsen, "Improving the pole relocating properties of vector fitting," *IEEE Transactions on Power Delivery*, vol. 21, no. 3, pp. 1587-1592, Jul. 2006.

[34] W. Tang, Q. Liang, B. Zhao *et al*., "Short-circuit fault classification method for AC submarine cables in offshore wind farms based on improved sparse representation," *Proceedings of the CSEE*, vol. 43, no. 6, pp. 2212-2222, Mar. 2023.

Xiaoping Gao received the B.S. and M.S. degrees in electrical engineering from Shanghai Jiao Tong University, Shanghai, China, in 2018 and 2021, respectively. He is currently pursuing the Ph.D. degree in electrical engineering at Xi'an Jiaotong University, Xi'an, China. His research interests include protection and control of renewable energy systems.

Guobing Song received the Ph. D. degree in electrical engineering from Xi'an Jiaotong University, Xi'an, China, in 2005. He is currently a Professor with the School of Electrical Engineering, Xi'an Jiaotong University. He is the Chairman of the DC Grid Protection Special Committee of IEEE PES (China) Power System Protection and Control Committee. His research interests include fault location, protection, and power electronics in power systems.

Xiaoning Kang received the Ph. D. degree in electrical engineering from Xi'an Jiaotong University, Xi'an, China, in 2006. He is currently a Professor with the School of Electrical Engineering, Xi'an Jiaotong University. His research interests include fault location, substation automation, and transformer protective relaying.

Can Cui received the B.S. degree in electrical engineering from Xi'an Jiaotong University, Xi'an, China, in 2024. He is currently pursuing the M. S. degree in electrical engineering at Xi'an Jiaotong University. His research interests include protection and control of inverter-based power systems.

Jifei Yan received the B.S. degree in electrical engineering from Xi'an Jiaotong University, Xi'an, China, in 2020. He is currently pursuing the Ph. D. degree in electrical engineering at Xi'an Jiaotong University. His research interests include fault location and protection of transmission lines.